*J Mater Sci: Mater Electron* (2025) 36:2195

# Optimizing the high-frequency magnetic properties of Fe-based nanocrystalline soft magnetic composites by incorporating carbonyl iron powder

Changlong Jin[1], Yanzhou Fan[1], Xingyu Zheng[1], Min Wang[1], Jifeng Zhou[1], Qiang Luo[1,*], Zhijun Guo[1,*], and Baolong Shen[1]

[1] *School of Materials Science and Engineering, Jiangsu Key Laboratory for Advanced Metallic Materials, Southeast University, Nanjing 211189, China*

**Received:** 6 October 2025
**Accepted:** 22 November 2025



## ABSTRACT

Novel Fe-based nanocrystalline soft magnetic composites (SMCs) are prepared using a cold pressing method with $Fe_{73.3}P_5Si_{7.6}B_{9.5}C_{1.9}Nb_2Cu_{0.7}$ powder and carbonyl iron powder (CIP). This work systematically explores the effect of adding CIP on both the microstructural development and the enhancement of soft magnetic performance. The optimized SMCs containing 15 wt.% CIP exhibit the most desirable soft magnetic properties subjected to appropriate heat treatment. Compared to its CIP-free core, the saturation magnetization ($M_s$) increases from 138 emu/g to 155 emu/g, and the effective permeability ($\mu_e$) rises from 45 to 53.6. The DC-bias characteristics reach 63% at 100 Oe, and the core loss ($P_{cv}$) decreases by ~ 20% to as low as 178 mW/cm$^3$ (0.05 T, 100 kHz). The improvement arises from CIP-induced densification that suppresses porosity and reduces domain-wall pinning. This unique combination of high permeability, robust DC-bias characteristics, and low core loss highlights the promise of CIP-doped nanocrystalline SMCs for high-current applications in advanced electronic and power devices.

## 1 Introduction

Innovations in wide-bandgap (WBG) semiconductors and new energy technologies are pushing electronic components toward miniaturization, higher operating frequencies, and greater current capacities. Consequently, stricter requirements have been imposed on the soft magnetic materials that are used as energy conversion components [1–3]. SMCs are composed of ferromagnetic powders and insulating materials that form a distributed air gap structure, which combines low eddy currents with shapeable form factors. Owing to their excellent soft magnetic properties, they are widely employed as key components in power electronic systems, such as inductors, transformers, filters, and switching power supplies [1, 4, 5]. To meet this developmental trend, the fabrication of SMCs that possess a combination of high $M_s$, high $\mu_e$, low $P_{cv}$, and excellent DC-bias characteristics is imperative [6, 7].

In 1988, the development of FeSiBNbCu nanocrystalline soft magnetic materials was first reported by Yoshizawa et al. [8]. The excellent overall soft magnetic

Address correspondence to E-mail: q.luo@seu.edu.cn; zj-guo@seu.edu.cn

https://doi.org/10.1007/s10854-025-16276-8
Published online: 01 December 2025

properties of these materials, which stem from their distinct amorphous-nanocrystalline dual-phase microstructure, make them promising candidates for the fabrication of SMCs [9–11]. However, a primary limitation of conventional atomization techniques is the restricted cooling rate. The incorporation of certain metalloid elements is necessary to promote the alloy's glass-forming ability (GFA) [12, 13]. As a result, nanocrystalline SMCs fabricated from these Fe-based amorphous alloy powders exhibit a lower $M_s$ compared to traditional powder cores (e.g., pure Fe or FeSi) [4, 14, 15]. Furthermore, the requisite insulation coating introduces non-magnetic phases and porosity, which in turn further degrades the composite's $\mu_e$ and $M_s$ [16]. Reported optimization routes include hot pressing[17], ultrasonic molding [18], magnetic field annealing [19], and secondary magnetic powders doping [20]. The latter is particularly attractive: Among these methods, fine soft magnetic dopants can occupy interparticle voids, raise green density, and are compatible with simple, low-cost processing [21, 22]. For instance, Zhang et al. [23] optimized the DC-bias characteristics and $M_s$ of FeSiBPNbCr amorphous SMCs by incorporating FeCo alloy powder. Wang et al. [21] improved the $\mu_e$ and DC-bias characteristics of FeSiBCCr amorphous SMCs while reducing $P_{cv}$ by doping with micron-sized FeSi powder. Song et al. [24] reported that the addition of FeNi powder to FeSiBCuNb nanocrystalline SMCs effectively enhanced the material's soft magnetic properties, leading to increased $\mu_e$ and lowered $P_{cv}$.

Carbonyl iron powder (CIP) is especially appealing as a dopant due to its small particle size, high ductility, excellent DC-bias performance, and intrinsic high $M_s$ [25–27]. The incorporation of an appropriate amount of CIP (average particle size: 4.75 μm) into FeSiCr powder has been established as an effective strategy to simultaneously elevate the density and optimize the soft magnetic properties [28]. Zhang et al. [29] enhanced the $\mu_e$ and DC-bias characteristics and reduced the $P_{cv}$ of FeSiBC amorphous SMCs by adding a suitable amount of CIP. Similarly, Wang et al. [22] effectively increased the density and optimized the $\mu_e$ and $P_{cv}$ of FeSiBCuNb nanocrystalline SMCs by doping with an appropriate amount of CIP. Building upon our prior work, we previously developed the $Fe_{73.3}P_5Si_{7.6}B_{9.5}C_{1.9}Nb_2Cu_{0.7}$ alloy, which exhibits both high GFA and excellent soft magnetic properties [30] compared with conventional Finemet alloy. Nonetheless, further improvement in $M_s$ is essential to meet the requirements of modern high-current and high-frequency applications. In this study, we proposed a dual-function strategy that incorporates fine CIP particles into $Fe_{73.3}P_5Si_{7.6}B_{9.5}C_{1.9}Nb_2Cu_{0.7}$ powders to simultaneously enhance $M_s$ and tune the microstructure. The CIP acts both as a high-$M_s$ magnetic constituent and as a microstructural regulator, mitigating porosity, relieving internal stress, and influencing domain-wall motion.

Accordingly, a series of $Fe_{73.3}P_5Si_{7.6}B_{9.5}C_{1.9}Nb_2Cu_{0.7}$/CIP SMCs containing 0–25 wt.% CIP were fabricated and systematically analyzed to elucidate how CIP governs microstructure and soft-magnetic performance. The findings indicate that an intermediate CIP fraction optimizes densification and magnetic response, delivering the best overall trade-off among $M_s$, $\mu_e$, $P_{cv}$, and DC-bias.

## 2 Experimental procedures

The synthesis of the $Fe_{73.3}P_5Si_{7.6}B_{9.5}C_{1.9}Nb_2Cu_{0.7}$ alloy ingots was carried out via induction melting in an argon atmosphere. The precursors included high-purity Fe (99.99 wt.%), Si (99.99 wt.%), B (99.99 wt.%), Nb (99.99 wt.%), Cu (99.99 wt.%), in addition to Fe–P (26.4 wt.% P) and Fe–C (5 wt.% C) master alloys.. The powder was synthesized through gas atomization with an atomization pressure of 8 MPa. Commercial CIP with a 5 μm average particle size was then blended with the gas-atomized FePSiBCNbCu soft magnetic powder (pre-sieved through 270-mesh). The CIP content in the final mixtures was systematically varied as follows: 0, 5, 10, 15, 20, and 25 wt.%. The powder mixture underwent mechanical alloying using a QM3SP04L planetary ball mill for 0.5 h. The homogenized powder was dispersed in an acetone-epoxy resin (2 wt.%) solution and mechanically stirred until the complete evaporation of the solvent was achieved. A subsequent vacuum drying step was performed on the as-coated powder at 60 °C for 1 h. The dried powder was then uniaxially pressed at 1800 MPa for 60 s, by which toroidal cores with outer diameter of 12.7 mm and inner diameter of 7.6 mm were formed. The final step was a heat treatment to promote nanocrystallization, for which the as-prepared cores were sealed under vacuum in quartz tubes and annealed at 480 °C for 30 min.

X-ray diffraction (XRD; Bruker D8 Focus) was utilized for the phase analysis of the original and

oxidized powders. For microstructural observation, a scanning electron microscope (SEM; Zeiss Rossbeam 350) was used to examine both the powders and the SMCs. The powder particle size distribution was analyzed with a laser diffraction analyzer (Mastersizer 3000, Malvern, UK). The Archimedes' principle was applied to measure the density and open porosity of the compacted cores. For magnetic characterization, a vibrating sample magnetometer (VSM; Lakeshore 707) was employed to measure the hysteresis loops at a maximum field of 800 kA/m. An impedance analyzer (Keysight, E4990A) was used to assess the complex permeability over the 10 kHz-120 MHz frequency range. The DC-bias characteristics were determined with an LCR meter (TongHui TH2828A) by tracking the $\mu_e$% up to 100 Oe. Lastly, a B-H analyzer (SY-8218, IWATSU) was used to quantify the $P_{cv}$ from 10 to 100 kHz.

## 3 Results and discussion

### 3.1 Microstructure analysis of FePSiBCNbCu alloy powder and carbonyl iron powder

The micro-morphologies of CIP and gas-atomized FePSiBCNbCu alloy powder are presented in Fig. 1(a,b). The morphology of CIP particles is predominantly spherical with a minor fraction of satellite particles, which arise from collisions and subsequent adhesion of droplets powders of different sizes during solidification [31]. In contrast, the FePSiBCNbCu powder exhibits higher sphericity and smoother surfaces (Fig. 1b), features that favor uniform insulation coating in subsequent processing. Particle size distributions (Fig. 1c) are near-normal for both materials. CIP spans the particle size range of 1–10 μm with D50 = 5.5 μm, whereas FePSiBCNbCu powder is coarser (6–125 μm, D50 = 33.4 μm). This significant difference in particle size was a deliberate design choice, as enhanced compaction efficiency can be achieved by mixing powders with controlled size disparities [32]. This deliberately bimodal sizing enhances packing efficiency: in close-packed assemblies of large spheres (diameter D), the tetrahedral and octahedral interstices admit smaller spheres (diameter d) only when d/D ≤ 0.225 (tetrahedral) and d/D ≤ 0.414 (octahedral), respectively. The measured D50 ratio for CIP to FePSiBCNbCu (0.164) satisfied these theoretical criteria, indicating that the interstitial spaces within the FePSiBCNbCu alloy powder matrix can be effectively occupied by the finer CIP particles. Through this particle size engineering strategy, both an enhancement in

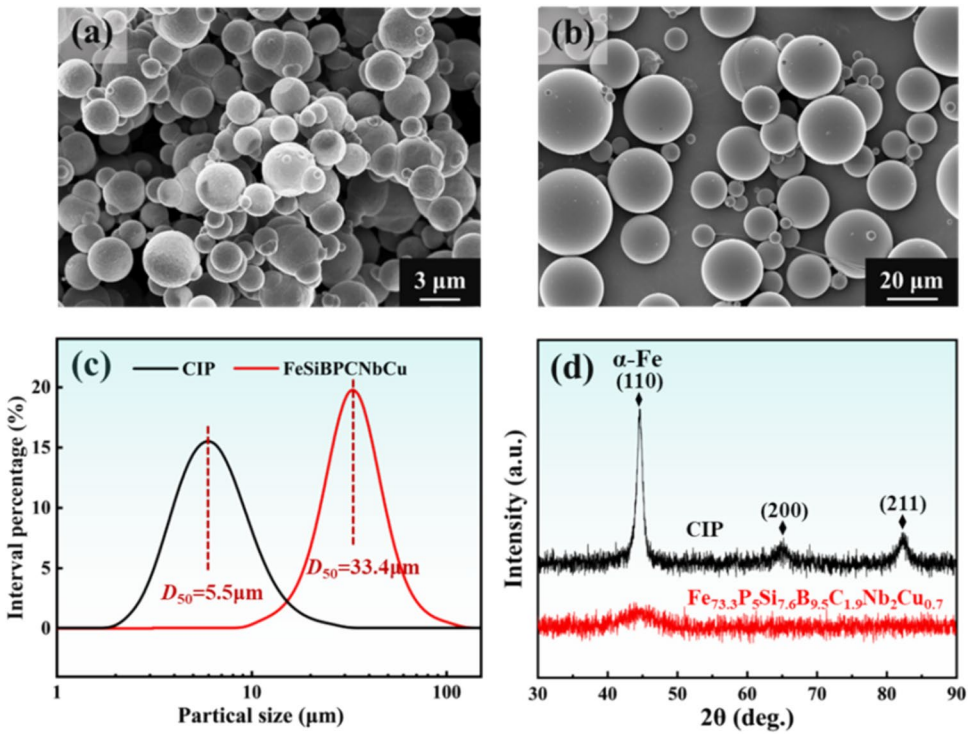


**Fig. 1** **a** SEM micrographs of CIP, **b** SEM micrographs of FePSiBCNbCu alloy powder, **c** particle size distribution of CIP and FePSiBCNbCu alloy powder. **d** XRD patterns of CIP and FePSiBCNbCu alloy powder

density and a decrease in porosity in the final composites are expected. The X-ray diffraction (XRD) patterns (Fig. 1d) confirm three $\alpha$-Fe reflections for CIP ((110), (200), and (211)), whereas FePSiBCNbCu alloy powder displays a single broad diffuse halo centered at $2\theta = 45.1°$, characteristic of a fully amorphous structure.

### 3.2 Density and microstructure of FePSiBCNbCu/CIP SMCs

The density of soft magnetic composites is considered a crucial performance indicator, as a higher density generally correlates with improved magnetic properties. As the CIP content was raised from 0 to 15 wt.%, the density of the as-fabricated FePSiBCNbCu/CIP SMCs was found to increase monotonically, a trend which is plotted in Fig. 2. A maximum density of ~ 5.7 g/cm$^3$ is achieved in the range of 15–20 wt.% CIP. A slight degradation in density was observed once the CIP content was raised above the optimal range. For the sample containing 25 wt.% CIP, a value of approximately 5.66 g/cm$^3$ was measured. The porosity of the SMCs exhibits an inverse trend relative to the density. This observed phenomenon can be ascribed to two primary factors. First, fine CIP particles fill the interstitial voids between the coarser FePSiBCNbCu particles, reducing the porosity and improving packing efficiency. Second, the true density of CIP (≈7.8 g/cm$^3$) exceeds that of the FePSiBCNbCu alloy powder (≈7.29 g/cm$^3$), further elevating the bulk density [27]. Beyond 20 wt.% CIP doping, excess fine particles tend to agglomerate, re-introducing porosity and decreasing the effective packing efficiency[16, 21].

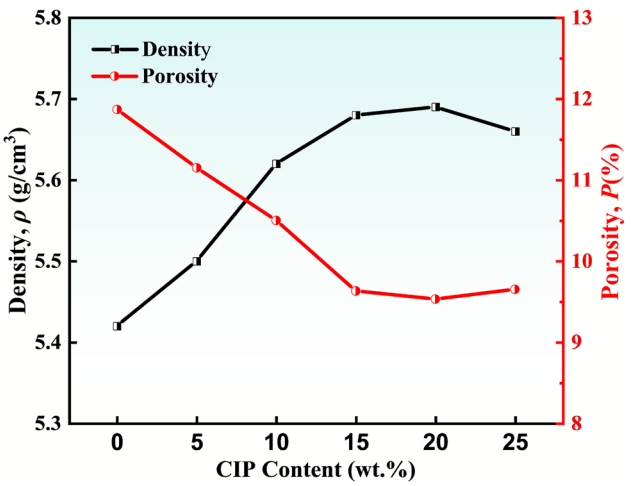


**Fig. 2** Density and porosity of FePSiBCNbCu/CIP SMCs as function of CIP contents

Fracture SEM micrographs (Fig. 3) corroborate these interpretations. In the CIP-free core (0 wt.%), large non-magnetic pores are distributed throughout the microstructure (red arrows in Fig. 3a), consistent with the measured density of ≈5.42 g/cm$^3$ and with increased domain-wall pinning. From a magnetic perspective, the pores within the composite are known to function as pinning sites. Consequently, domain wall motion during magnetization is hampered by these sites, and improvement in the comprehensive soft magnetic properties is thereby impaired. Introducing 5–15 wt.% CIP facilitates interstitial filling between coarse FePSiBCNbCu alloy powder particles (orange dashed boxes in Fig. 3b, c), thereby reducing porosity and raising density. At 25 wt.% CIP, agglomeration of the surplus fine particles becomes evident (blue dashed boxes in Fig. 3d), increasing interparticle interfaces and creating additional microvoids, which account for the modest density decrease.

### 3.3 Magnetic performance of FePSiBCNbCu/CIP SMCs

Hysteresis loops for FePSiBCNbCu/CIP SMCs with 0–25 wt.% CIP (Fig. 4) reveal a progressive increase in high-field magnetization with CIP addition. FePSiBCNbCu/CIP The CIP-free core exhibits $M_s = 138$ emu/g. Because CIP possesses a high intrinsic saturation magnetization (≈ 216.5 emu/g)[27], $M_s$ rises monotonically with CIP content, reaching about163 emu/g at 25 wt.%. The DC-bias characteristics (Fig. 5) show the expected FePSiBCNbCu/CIP decrease of percent permeability ($\mu_e$%) with increasing applied DC field. At 100 Oe, $\mu_e$% varies in a non-monotonic trend with CIP content: 58% (0 wt.%), 57% (5 wt.%), then generally higher values with additional CIP, namely, ~ 63% (15 wt.%), ~ 66% (20 wt.%), and ~ 70% (25 wt.%). This initial drop at 5 wt.% CIP is attributed to the fact that the detrimental impact from the relatively large increase in $\mu_e$ on DC-bias characteristics outweighs the positive contribution from the enhanced $M_s$ [22, 23].With further CIP, the increased value of $M_s$ delays saturation and improves $\mu_e$% under the same bias field. Concurrent densification also mitigates demagnetizing effects, contributing to the overall improvement.

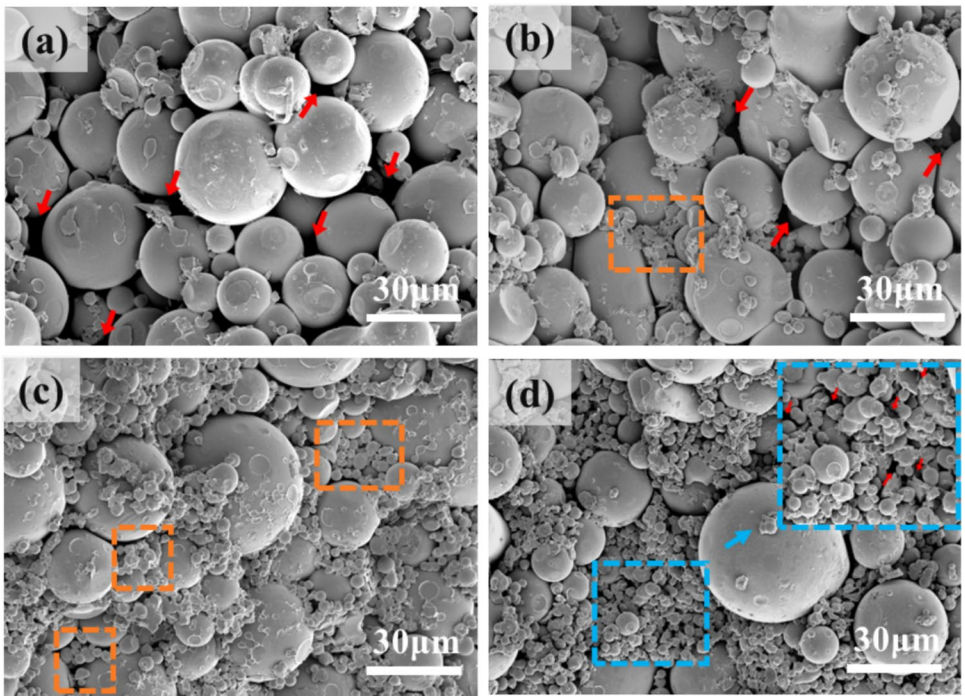


**Fig. 3** Fracture SEM morphology of the FePSiBCNbCu/CIP SMCs doped with different CIP contents, **a** 0 wt.% (red arrows: large pores), **b** 5 wt.% and **c** 15 wt.% (orange dashed boxes: interstitial filling by CIP), **d** 25 wt.% (blue dashed boxes: CIP particles agglomerate and associated microvoids)

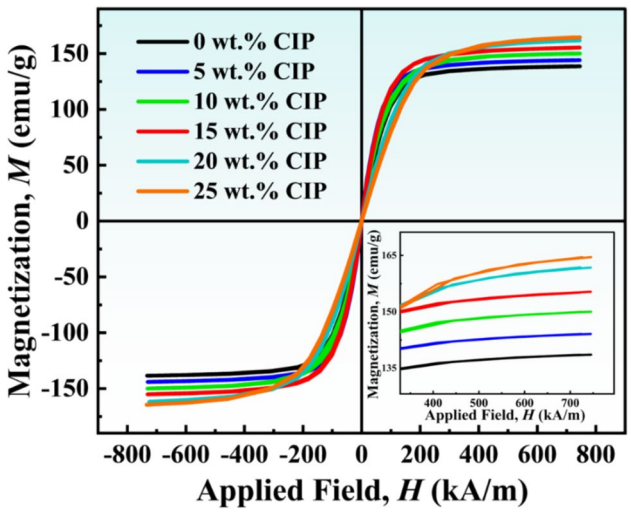


**Fig. 4** Hysteresis loops of FePSiBCNbCu/CIP SMCs doped with different content of CIP

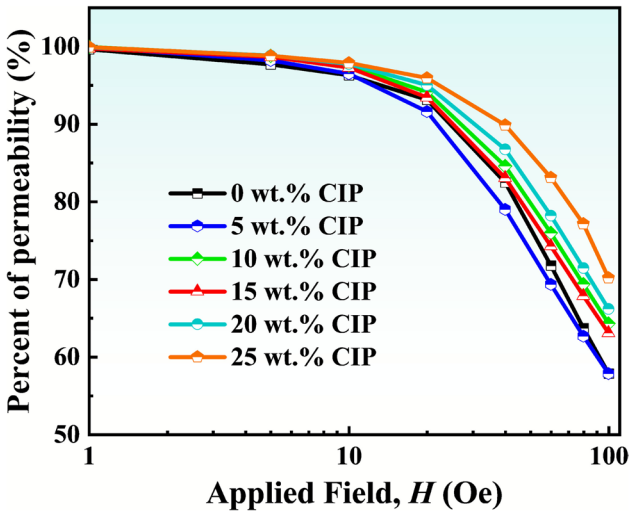


**Fig. 5** DC-bias characteristics of FePSiBCNbCu/CIP SMCs as a function of applied DC field difference, measured for various CIP contents (0–25 wt.%)

The dependence of the $\mu_e$ on frequency for FePSiBCNbCu/CIP SMCs is presented in Fig. 6. For all prepared samples, stable $\mu_e$ values up to a frequency of 10 MHz were observed, indicating excellent frequency stability. A non-monotonic relationship between the $\mu_e$ and the CIP content was also found. Initially, the progressive enhancement of the $\mu_e$ was driven by the increase in CIP content from 0 wt.% to 15 wt.%, reaching a maximum value of approximately 53.6, which is an increase from the initial value of ~ 45. However, a further increase in the CIP content to 20 wt.% resulted in a significant reduction in $\mu_e$, with a value of ~ 47 being recorded for this sample. With a further increase to 25 wt.% CIP, a $\mu_e$

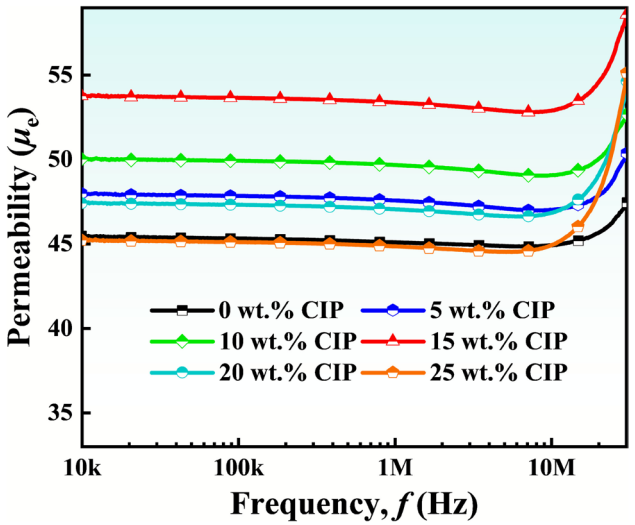


**Fig. 6** Frequency-dependence of the effective permeability ($\mu_e$) of FePSiBCNbCu/CIP SMCs doped with different CIP contents

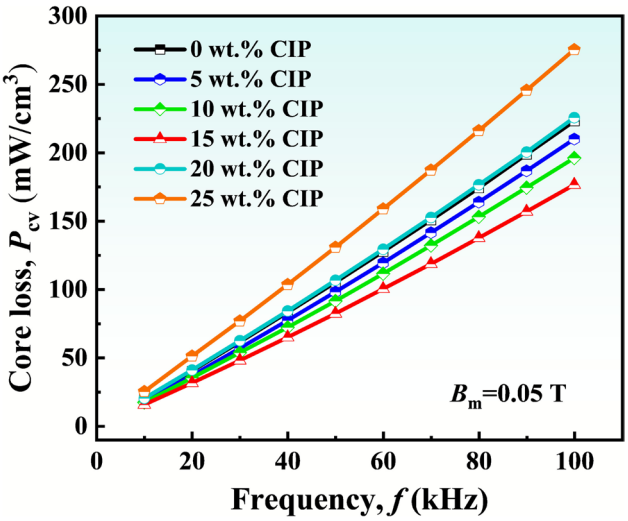


**Fig. 7** Frequency-dependence of the core loss ($P_{cv}$) of the SMCs doped with different CIP contents

value even lower than that of the pure FePSiBCNbCu SMCs (0 wt.% CIP) was obtained.

To explain this phenomenon, a systematic analysis considering both density and average particle size effects in the SMCs is necessary. The empirical relationship governing the $\mu_e$ of such composites, originally derived from Visser's powder continuity model [33], can be expressed as follow:

$$\mu' = \frac{\mu_i d}{\mu_i \delta + d} \tag{1}$$

where $\mu_i$, $d$, and $\delta$ are the intrinsic complex permeability, the average powder particle diameter, and the non-magnetic phase volume fraction (e.g., porosity), respectively. The $\mu_e$ enhancement mechanism through CIP addition (up to 20 wt.%) can be interpreted through Eq.(1): The initial improvement in $\mu_e$ with increasing CIP content can be explained by two primary factors. First, the overall porosity of the composite is reduced by the incorporation of fine CIP particles. As a result of the decreased non-magnetic phase volume fraction, the magnetic reluctance effect is weakened, and an enhancement in $\mu_e$ is consequently facilitated [34]. Second, a positive contribution to the $\mu_e$ is also made by the increase in the overall $M_s$ of the composite. Conversely, at CIP concentrations of 20 wt.% and above, the $\mu_e$ was found to decrease. This phenomenon is likely caused by the agglomeration of the fine CIP particles. As is shown in Fig. 3d, this agglomeration creates new, smaller air gaps, which increases the overall porosity. As a consequence, the process of domain wall motion between particles is obstructed during magnetization[35].

The dependence of the $P_{cv}$ on frequency for FePSiBCNbCu/CIP SMCs with various CIP contents is presented in Fig. 7. The measurements were performed over a frequency range of up to 100 kHz while maintaining a constant magnetic induction (Bm) of 0.05 T. For all compositions, a monotonic increase in $P_{cv}$ as a function of frequency was observed. However, a non-monotonic relationship between $P_{cv}$ and the CIP content was also noted. As the CIP content was increased from 0 to 25 wt.%, the $P_{cv}$ was first observed to decrease, reaching a minimum, before subsequently rising. A minimum core loss of 178 mW/cm$^3$ (at 100 kHz, 0.05 T) was obtained for the sample containing 15 wt.% CIP, which underscores the significant influence of composition on loss reduction.

The classical loss separation model, as proposed by Bertotti [36] and Kollar [37], defines the $P_{cv}$ as the sum of three components: hysteresis loss ($P_h$), eddy current loss ($P_e$), and residual loss ($P_{exc}$). In the present study, this loss separation model was employed to investigate the mechanism by which powder doping influences $P_{cv}$. This decomposition can be described by the following equation:

$$P_{cv} = P_h + P_e + P_{exc} \tag{2}$$

$$P_{cv} = C_h B_m^{\alpha} f + C_e B_m^2 f^2 + C_{exc} B_m^x f^y \tag{3}$$

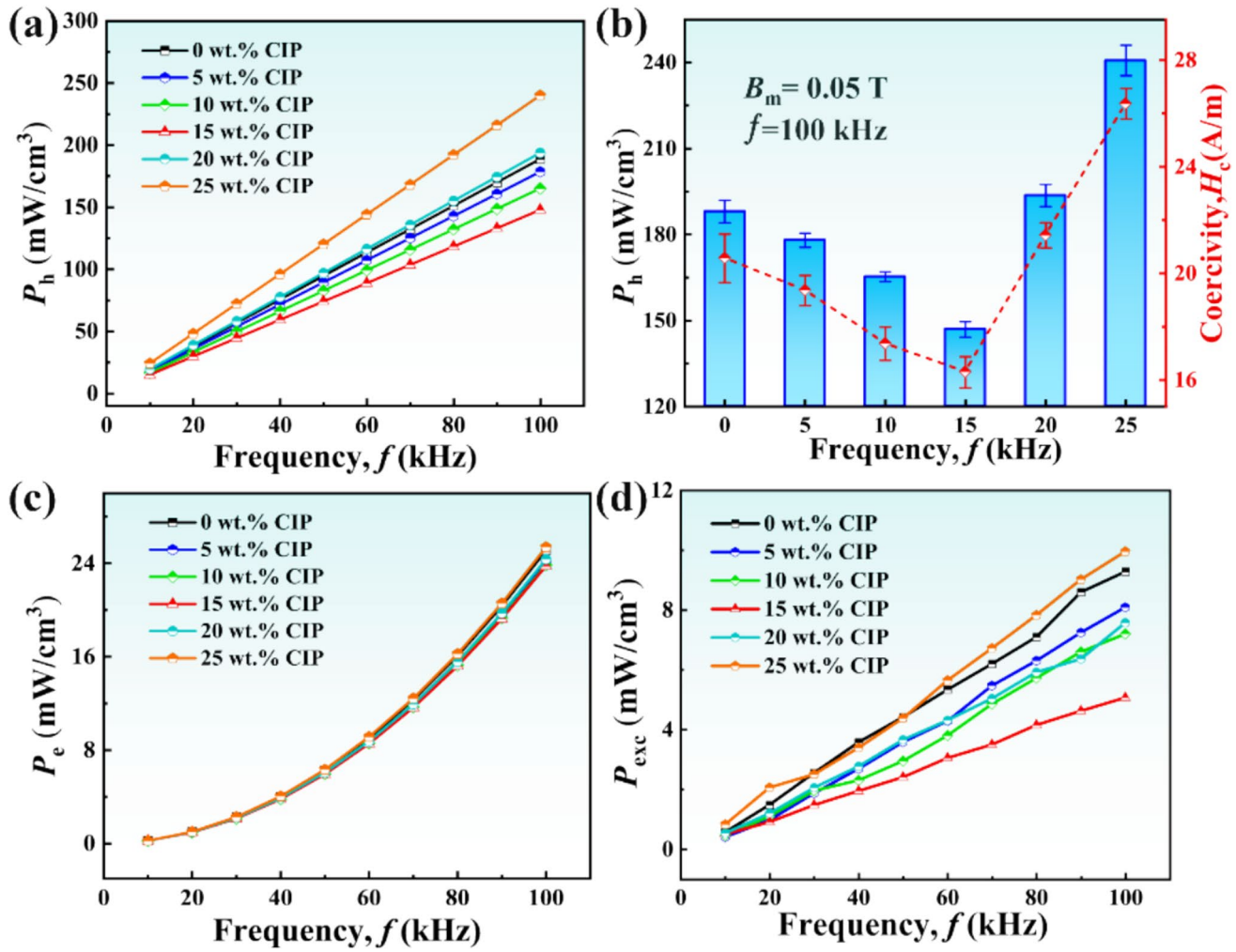


**Fig. 8** Frequency-dependent of (a) hysteresis loss ($P_h$), (c) eddy current loss ($P_e$), and (d) excess loss ($P_{exc}$) of the SMCs doped with different CIP contents; (b) histogram of $P_h$ and $H_c$ at 0.05 T and 100 kHz

where $f$ is the frequency, and the parameters $C_h$, $C_e$, and $C_{exc}$ are the respective coefficients for hysteresis, eddy current, and excess losses.

As is shown by the loss separation results plotted in Fig. 8(a, c, d), the $P_{cv}$ is predominantly determined by the $P_h$ component over the 0–100 kHz frequency range for all SMCs with varying CIP content. Figure 8(b) further demonstrates that $P_h$ exhibits a non-monotonic trend with increasing CIP content, decreasing at first and then increasing, with a minimum at 15% CIP. Because of coercivity ($H_c$) critically governs $P_h$. $H_c$ exhibits a similar non-monotonic trend and likewise reaches a minimum value at 15 wt.%CIP. The simultaneous reduction in $H_c$ and $P_h$ originates from densification driven by CIP incorporation. Fine CIP particles effectively fill interparticle voids, thereby reducing porosity. Because pores act as domain wall pinning sites and sources of strong local demagnetizing fields [16], their elimination weakens these internal demagnetizing fields and alleviates pinning sites, facilitating domain wall motion and consequently lowering $H_c$ and $P_h$ [38, 39]. In addition, the reduced inter-particle spacing achieved through the packing of fine, ductile CIP promotes stronger magnetic exchange coupling across adjacent powder particles. Enhanced exchange interaction improves magnetization rotation coherence and magnetic flux transfer efficiency, between powder particles, further suppressing $H_c$ and $P_h$ [18, 40].

The frequency-dependent behavior of the $P_e$ can be observed in Fig. 8(c). Within the 100 kHz frequency range, FePSiBCNbCu/CIP decreases slightly at low CIP levels and then increases with further CIP

addition. However, it remains a minor contribution to $P_{cv}$ throughout this range. The observed behavior can be explained by a twofold mechanism. The first mechanism involves the suppression of intra-particle eddy current loss, which can be ascribed to the decrease in the average particle size brought about by the addition of fine CIP. The second, opposing factor is the enhancement of inter-particle eddy currents, which can be attributed to the lower resistivity of CIP relative to the FePSiBCNbCu powder [41]. The frequency-dependent behavior of the $P_{exc}$ can be observed in Fig. 8(d). A strong correlation between the $P_{exc}$ and the $P_h$ was observed. This correlation is an expected outcome, as the residual loss is known to be strongly influenced by factors such as density and the non-magnetic phase volume fraction [16].

The comprehensive properties of the FePSiBCNbCu/CIP SMCs with different CIP doping amounts are summarized in Table 1. Compared to CIP-free FePSiBCNbCu SMCs, adding an appropriate fraction of fine CIP fills interstitial voids between the primary powder particles, thereby reducing porosity and improving packing. As a result, $P_{cv}$ decreases and effective $\mu_e$ increases. When the CIP content exceeds a threshold, fine particles agglomeration introduces additional interparticle interfaces and porosity, which deteriorate soft magnetic properties. By considering the trade-off between the $\mu_e$, DC-bias characteristics, and $P_{cv}$, it was determined that the most favorable combination of soft magnetic properties was exhibited by the sample with 15 wt.% CIP.

Benchmarking against representative SMCs from the literature (Table 2) shows that the FePSiBCNbCu /15 wt.% CIP SMCs developed in this work exhibit a superior balance of soft-magnetic properties[7, 21, 22, 27, 42, 43]. It combines an $\mu_e$ of 53.6 (100 kHz) with strong DC-bias characteristics (63% at 100 Oe) and a low $P_{cv}$ of 178 mW/cm$^3$ (0.05 T, 100 kHz), while maintaining $M_s$ = 155 emu/g. The results of this work indicate that the control of the non-magnetic phase volume fraction, which can be achieved through the careful engineering of the powder microstructure, is an effective strategy for the enhancement of the overall soft magnetic properties of these composites.

**Table 1** Summary of key physical and magnetic properties for FePSiBCNbCu/CIP SMCs with varying CIP content

| CIP content( wt.%) | Density ( g/cm$^3$) | $M_s$ ( emu/g) | $\mu_e$ 100 kHz | DC-Bias ( %) 100 Oe | $P_{cv}$ ( mW/cm$^3$) 50 mT, 100 kHz |
|---|---|---|---|---|---|
| 0 | 5.42 | 138 | 45.3 | 58 | 223 |
| 5 | 5.50 | 144 | 47.8 | 57 | 210 |
| 10 | 5.62 | 150 | 49.9 | 64 | 196 |
| 15 | 5.68 | 155 | 53.6 | 63 | 178 |
| 20 | 5.69 | 162 | 47.3 | 66 | 226 |
| 25 | 5.66 | 164 | 45.1 | 70 | 275 |

**Table 2** Comparison of key performance metrics for the FePSiBCNbCu/CIP SMCs developed in this study versus those of other representative SMCs

| Materials | Forming pressure MPa | $\mu_e$ 100 kHz | DC-Bias (%) 100 Oe | $P_{cv}$(mW/cm$^3$) 0.05 T, 100 kHz | $M_s$ (emu/g) | Reference |
|---|---|---|---|---|---|---|
| FePSiBCNbCu/15 wt.% CIP@EP | 1800 | 53.6 | 63 | 178 | 155 | This work |
| FeSiB/FeNi@SI | 1400 | 31 | | 350 | 157.7 | [7] |
| FeSiBCr/CIP@EP | 100 | 32.1 | 78 | | 149.1 | [20] |
| FeSiBC/CIP@EP | 1800 | 34.9 | 76 | 325.72 | 179.5 | [42] |
| FeSiBCuNb/FeNi@$HNO_3$ | 1200 | 57.4 | 61.8 | 260 | 136.3 | [43] |
| FeSiBCuNb/CIP@Phosphate | 600 | 35.3 | | 281.8 | 158.5 | [22] |
| FeSiBPCMo/CIP@$SiO_2$ | 500 | 35.7 | 79 | 263.9 | | [27] |

## 4 Conclusion

The role of CIP doping in enhancing the soft magnetic properties of Fe-based nanocrystalline SMCs was elucidated in the present study. The $M_s$ is significantly improved by the incorporation of CIP, reaching 164 emu/g at 25 wt.% CIP, representing a 19% increase compared to the CIP-free composite. Moderate CIP addition effectively fills the interstitial voids between primary amorphous powder particles, increasing compacted density and reducing pinning sites for domain wall motion. However, excessive CIP leads to particle agglomeration and higher interfacial porosity, thereby deteriorating the soft magnetic properties. The obtained SMC containing 15 wt.% CIP achieves the best overall soft magnetic properties, exhibiting $M_s$ of 155 emu/g, $\mu_e$ of 53, a DC-bias characteristic of 63% (100 Oe), and a low $P_{cv}$ of 178 mW/cm$^3$ (0.05 T, 100 kHz). Overall, this study demonstrates that engineering the powder microstructure through controlled CIP addition provides a robust strategy for achieving excellent overall performance in nanocrystalline SMCs.

## Acknowledgements

This work was financially supported by the National Key R&D Program of China (No. 2022YFB3804100), the National Natural Science Foundation of China (No. 52231005), the Natural Science Foundation of Jiangsu Province (No. BK20221474), the Start-up Research Fund of Southeast University (No. RF1028623113), the Science Technology Development Program of Yixing (No. C2024002).

## Author contributions

CJ: Data curation, Formal analysis, Investigation, Writing—original draft. YF: Data curation, Formal analysis, Investigation. XZ: Data curation, Investigation. MW: Formal analysis. JZ: Investigation. QL: Formal analysis. ZG: Funding acquisition, Methodology, Writing—review & editing. BS: Funding acquisition, Supervision, Project administration, Writing—review & editing.

## Data availability

Data will be made available on request.

## Declarations

**Conflict of interest** The authors declare no competing interests.

## References

1. J.M. Silveyra, E. Ferrara, D.L. Huber, T.C. Monson, Science (2018). https://doi.org/10.1126/science.aao0195
2. W.C. Li, H.W. Cai, Y. Kang, Y. Ying, J. Yu, J.W. Zheng, L. Qiao, Y. Jiang, S.L. Che, Acta Mater. (2019). https://doi.org/10.1016/j.actamat.2019.01.035
3. M. Jiang, J. Wang, M. Cai, J. Li, W. Dong, Z. Guo, B. Shen, J. Non-Cryst. Solids (2025). https://doi.org/10.1016/j.jnoncrysol.2024.123382
4. J.Y. He, H. Yuan, M. Nie, H. Guo, H.Y. Yu, Z.W. Liu, R. Sun, Mater. Today Electron. (2023). https://doi.org/10.1016/j.mtelec.2023.100066
5. E.A. Périgo, B. Weidenfeller, P. Kollár, J. Füzer, Appl. Phys. Rev. (2018). https://doi.org/10.1063/1.5027045
6. H.I. Hsiang, L.F. Fan, J.J. Hung, J. Magn. Magn. Mater. (2018). https://doi.org/10.1016/j.jmmm.2017.08.096
7. B. Li, Z. Zheng, H.Y. Yu, D. Zeng, J. Magn. Magn. Mater. (2017). https://doi.org/10.1016/j.jmmm.2017.04.082
8. Y. Yoshizawa, S. Oguma, K. Yamauchi, J. Appl. Phys. (1988). https://doi.org/10.1063/1.342149
9. G. Herzer, IEEE Trans. Magn. (1990). https://doi.org/10.1109/20.104389
10. G. Herzer, Scr. Metall. Mater. (1995). https://doi.org/10.1016/0956-716X(95)00397-E
11. Y.P. Liu, Y.D. Yi, W. Shao, Y.F. Shao, J. Magn. Magn. Mater. (2013). https://doi.org/10.1016/j.jmmm.2012.10.043
12. Y.Z. Fan, C.L. Jin, M. Wang, J.F. Zhou, J.H. Fu, D. Li, Q. Luo, Z.J. Guo, B.L. Shen, J. Alloys Compd. (2025). https://doi.org/10.1016/j.jallcom.2025.184627
13. M.J. Cai, Z.J. Guo, L. Li, X.Y. Zheng, X.X. Yang, Q.Q. Liu, G.P. Zou, B.L. Shen, J. Mater. Sci. Technol. (2025). https://doi.org/10.1016/j.jmst.2024.04.047
14. L.X. Shi, K.F. Yao, Mater. Des. (2020). https://doi.org/10.1016/j.matdes.2020.108511
15. S.H. Lu, M.G. Wang, Z.K. Zhao, J. Non-Cryst. Solids (2023). https://doi.org/10.1016/j.jnoncrysol.2023.122440

16. Z.L. Guo, J.H. Wang, W.H. Chen, D.C. Chen, H.B. Sun, Z.L. Xue, C. Wang, Mater. Des. (2020). https://doi.org/10.1016/j.matdes.2020.108769
17. M. Kuno, N. Ono, Y. Imano, A. Urata, H. Oikawa, S. Okamoto, Acta Mater. (2025). https://doi.org/10.1016/j.actamat.2025.121159
18. H.Z. Li, Y.Q. Yan, W.S. Cai, L.Y. Li, A. Yan, L.H. Liu, J. Ma, H.B. Ke, Q. Li, B.A. Sun, W.H. Wang, C. Yang, Nat. Commun. (2024). https://doi.org/10.1038/s41467-024-53592-9
19. M. Nie, C.Y. Jiang, W.Y. Song, M. Chen, J.Y. He, Z.Y. Chen, Z.C. Li, G.P. Jia, H. Guo, J. Alloys Compd. (2024). https://doi.org/10.1016/j.jallcom.2024.175995
20. H.J. Woo, S.W. Kim, C.P. Kim, D.H. Choi, S. Kim, B.W. Lee, J. Magn. Magn. Mater. (2023). https://doi.org/10.1016/j.jmmm.2022.170181
21. J.H. Wang, Z.L. Guo, Q.T. Zeng, G.H. Hang, Z.L. Xue, D.C. Chen, Z.K. Liang, H.B. Sun, J. Magn. Magn. Mater. (2020). https://doi.org/10.1016/j.jmmm.2020.166931
22. B. Wang, Z.S. Zhang, J.B. Shen, Y. Tian, B.X. Wang, L.W. Cai, L.D. Liu, Y.D. Yu, G.D. Wang, J. Alloys Compd. (2024). https://doi.org/10.1016/j.jallcom.2023.172812
23. Y.Q. Zhang, Q. Chi, L. Chang, Y.Q. Dong, P.P. Cai, Y. Pan, M.J. Gong, J.J. Huang, J.W. Li, A.N. He, X.M. Wang, J. Magn. Magn. Mater. (2020). https://doi.org/10.1016/j.jmmm.2020.166840
24. Y.Y. Song, S.X. Zhou, Z. Zhang, R.B. Zhang, X.T. Li, X.Y. Jing, J. Non-Cryst. Solids (2024). https://doi.org/10.1016/j.jnoncrysol.2024.123260
25. J.B. Shen, B. Wang, L.W. Cai, L.D. Liu, C. Zhang, B.X. Wang, Y. Tian, Y.D. Yu, J.Q. Dong, G.D. Wang, J. Mater. Sci. Mater. Electron. (2023). https://doi.org/10.1007/s10854-023-10512-9
26. Q.L. Chen, L.Y. Li, Z.L. Wang, Y.C. Ge, C.S. Zhou, J.H. Yi, J. Alloys Compd. (2019). https://doi.org/10.1016/j.jallcom.2018.11.112
27. H.R. Kim, M.S. Jang, Y.G. Nam, Y.S. Kim, S.S. Yang, Y.J. Kim, J.W. Jeong, Metals (2021). https://doi.org/10.3390/met11081220
28. C. Xia, Y.D. Peng, X.W. Yi, Z.X. Yao, Y.Y. Zhu, G. Hu, J. Non-Cryst. Solids (2021). https://doi.org/10.1016/j.jnoncrysol.2021.120673
29. Z. Zhang, X.R. Liu, Y.H. Jiang, B.B. Xing, W.J. Li, X.Y. Jing, P.X. Ge, R.B. Zhang, F. Xu, J. Mater. Sci. Mater. Electron. (2024). https://doi.org/10.1007/s10854-024-12183-6
30. Z.J. Guo, X.Y. Zheng, C.L. Jin, Y.Z. Fan, M.J. Cai, J.F. Zhou, W.Y. Dong, Q. Luo, B.L. Shen, Mater. Today Nano (2025). https://doi.org/10.1016/j.mtnano.2025.100621
31. S. Luo, H.Z. Wang, Z.Y. Gao, Y. Wu, H.W. Wang, Mater. Des. (2021). https://doi.org/10.1016/j.matdes.2021.110264
32. N. Yabu, K. Sugimura, M. Sonehara, T. Sato, IEEE Trans. Magn. (2018). https://doi.org/10.1109/TMAG.2018.2832662
33. M.T. Johnson, E.G. Visser, IEEE Trans. Magn. (1990). https://doi.org/10.1109/20.104592
34. C.T. Chang, J.J. Guo, Q. Li, S.M. Zhou, M. Liu, Y.Q. Dong, J. Alloys Compd. (2019). https://doi.org/10.1016/j.jallcom.2019.02.301
35. Y.Q. Dong, Z.C. Li, M. Liu, C.T. Chang, F.S. Li, X.M. Wang, Mater. Res. Bull. (2017). https://doi.org/10.1016/j.materresbull.2017.04.030
36. X.Y. Wang, Z.C. Lu, C.W. Lu, D.R. Li, J. Magn. Magn. Mater. (2013). https://doi.org/10.1016/j.jmmm.2013.07.043
37. H.H. Huang, R. Zhang, H.B. Sun, J.C. Zhang, J.H. Wang, J. Alloys Compd. (2023). https://doi.org/10.1016/j.jallcom.2023.169460
38. Y.Z. Fan, Z.J. Guo, M. Wang, C.L. Jin, J.F. Zhou, Y.Q. Dong, Q.K. Man, B.L. Shen, Sci. China Phys., Mech. Astron. (2025). https://doi.org/10.1007/s11433-025-2711-2
39. B. Zhou, Y.Q. Dong, L. Liu, L. Chang, F.Q. Bi, X.M. Wang, J. Magn. Magn. Mater. (2019). https://doi.org/10.1016/j.jmmm.2018.11.014
40. H.S. Liang, T. Hou, T.C. Liu, S.C. Hui, Z.Y. Hou, Z. Wang, B. Shi, L.M. Zhang, H. Shen, H.J. Wu, Carbon (2026). https://doi.org/10.1016/j.carbon.2025.120922
41. L. Chang, Y.Q. Zhang, Y.Q. Dong, Q. Li, A.N. He, C.T. Chang, X.M. Wang, SN Appl. Sci. (2019). https://doi.org/10.1007/s42452-019-0950-1
42. P. Wang, Z.Q. Zhu, J.Q. Liu, H. Zhao, J. Pang, J.Q. Zhang, J. Magn. Magn. Mater. (2023). https://doi.org/10.1016/j.jmmm.2023.170809
43. T. Feng, M. Cheng, Y.H. Li, Y.B. Zhang, L. Jiang, L. Yang, W. Zhang, Sci. China Phys., Mech. Astron. (2025). https://doi.org/10.1007/s11433-025-2684-4